frontiers | Frontiers in Materials

TYPE Original Research
PUBLISHED 13 March 2024
DOI 10.3389/fmats.2024.1353004

OPEN ACCESS

EDITED BY
Mizan Ahmed,
Curtin University, Australia

REVIEWED BY
Ping Duan,
China University of Geosciences Wuhan, China
Jun Ren,
Yunnan University, China

*CORRESPONDENCE
Yao Yue,
yueyao2019@yeah.net

RECEIVED 09 December 2023
ACCEPTED 26 February 2024
PUBLISHED 13 March 2024

CITATION
Yang G, Li C, Xie W, Yue Y, Kong C and Li X (2024), Effect of carbide slag and steel slag as alkali activators on the key properties of carbide slag-steel slag-slag-phosphogypsum composite cementitious materials. *Front. Mater.* 11:1353004. doi: 10.3389/fmats.2024.1353004

Effect of carbide slag and steel slag as alkali activators on the key properties of carbide slag-steel slag-slag-phosphogypsum composite cementitious materials

Guihong Yang[1], Chao Li[2], Wangshan Xie[2], Yao Yue[3]*, Chuiyuan Kong[4] and Xiaolong Li[5]

[1]China Railway Construction Kunlun Investment Group Co., Ltd., Kunming, China, [2]China Railway Construction Yunnan Investment Co., Ltd., Kunming, China, [3]Department of Highway and Architectural Engineering, Yunnan Communications Vocational and Technical College, Kunming, China, [4]Faculty of Civil Engineering and Mechanics, Kunming University of Science and Technology, Kunming, China, [5]Yunnan Provincial Institute of Highway Science Technology, Kunming, China

In order to enhance the utilization of alkaline carbide slag (CS) and steel slag (SS) in solid waste-based cementitious materials (SWBCM). In this study, slag (GGBS) was utilized as the primary material, phosphogypsum (PG) as the sulfat activator, and carbide slag (CS) and steel slag (SS) as the alkali activators to prepare carbide slag-steel slag-slag-phosphogypsum composite cementitious material (CS-SS-GGBS-PG). The impact of partial SS (mass fraction) substitution by CS on the flowability, mechanical properties, softening coefficient, pore solution pH value, hydration heat, and microstructure of CS-SS-GGBS-PG was studied. The hydration products, microstructure, and pore structure of CS-SS-GGBS-PG were studied via XRD, FTIR, TG-DTG, SEM, and MIP. The results show that CS replacement with SS decreases the flowability of CS-SS-GGBS-PG compared to the specimen without CS doping (A0). The addition of CS provides an abundance of Ca^{2+} and OH^{-} to facilitate the hydration reaction in the system, prompting CS-SS-GGBS-PG to form more C-(A)-S-H gels and ettringite (AFt) in the early stages. This significantly enhances the 3 and 7 days strength of CS-SS-GGBS-PG. Compared to A0, the sample group with 5% CS substitution for SS showed a respective increase of 400% and 1,150% in flexural strength at 3 and 7 days, and an increase of 800% and 1,633% in compressive strength. However, if CS is substituted for SS in excess, the system's late hydration process will be inhibited, increasing the volume of harmful pores in the specimen's microstructure and lowering its degree of compactness. This leads to a decrease of 28 days of strength and a deterioration of the water resistance of CS-SS-GGBS-PG. It is advised that the blending ratio of SS to CS be 3:1 in order to maintain equilibrium between the early strength enhancement of CS-SS-GGBS-PG and the stability of strength and water resistance in the latter stage. This study has a positive impact on improving the utilization of CS and SS in SWBCM, reducing the dependence of SWBCM on traditional

high-angstrom chemical alkali activators, and promoting the development of SWBCM.

KEYWORDS

carbide slag, steel slag, alkali activators, solid waste-based cementitious materials, mechanical properties, microstructure

1 Introduction

Cement is the most widely used cementitious material in the construction industry. Nevertheless, the production process of cement produces significant volumes of CO_2 emissions, which contribute around 6%–8% of the global carbon emissions (Wang et al., 2022c; Zhu et al., 2023). Such large-scale CO_2 emissions run counter to the "dual-carbon" targets proposed by various countries. Therefore, there is an urgent need for the traditional cement industry to transition to a low-carbon system for sustainability (Zhu et al., 2023). One successful way is to utilize industrial solid wastes to produce solid waste-based cementitious materials (SWBCM) to replace part of the cement used, which not only decreases the quantity of cement needed but also reduces carbon emissions directly and effectively.

SWBCM, as a new low-carbon cementitious material, has received increasing attention from researchers in recent years. Its basic materials mostly consist of industrial solid wastes such as phosphogypsum (PG), fly ash (FA), slag (GGBS), steel slag (SS), and others (Song et al., 2020; Liu et al., 2022). These solid wastes are produced and stockpiled in huge quantities, so the use of SWBCM to replace part of the use of cement is both effective in reducing the carbon emissions of the cement industry and helps to realize the resourcefulness of industrial solid wastes. However, the low strength of SWBCM (Zhu et al., 2023), especially the early strength, severely limits the popularization and application of SWBCM. The main reason for this is the low alkalinity of the system, which does not promote the hydration of potentially water-hardened solid wastes well. Current research is generally aimed at increasing the strength of SWBCM by adding chemical alkali activators, the most commonly used chemical alkali activators being caustic soda, potassium waterglass, sodium waterglass, mixtures of different chemical alkali activators, etc. (You et al., 2019; An et al.,2023; Song et al., 2020; Pang, 2021; Ren et al., 2023). Although chemical alkali activators are effective in developing the strength of SWBCM, they are not suitable for large-scale engineering applications due to their high price, high corrosiveness, and the high carbon emissions typically associated with their production (Vinai and Soutsos, 2019). Therefore, research to explore the use of low-cost solid waste activators as an alternative to traditional chemical alkali activators has become important.

According to reports, PG, SS, and carbide slag (CS) can all enhance the mechanical properties of SWBCM (Wang et al., 2023b; Wang et al., 2022d; Zhang et al., 2023). The major component of PG is calcium sulfate dihydrate ($CaSO_4{\cdot}2H_2O$), which is formed when phosphate ore is treated with sulfuric acid in the manufacturing of wet process phosphoric acid (Ma et al., 2021; Liu et al., 2022). SS is an alkaline solid waste produced during the ironmaking process. Its low activity, swelling, and compositional fluctuations make it difficult to utilize on a large scale (Zhang and Wang, 2021; Hao et al., 2022; Shu and Sasaki, 2022). CS is an alkaline waste material produced by the hydrolysis of calcium carbide for the manufacturing of C_2H_2 gas, PVC, and other products, with $Ca(OH)_2$(CH) as its major component. However, the presence of a number of difficult-to-treat impurities and hazardous components, such as acetylene gas, hydrogen sulfide, etc. (Zhang et al., 2019), makes it difficult to use CS in a secondary manner. Large stockpiles of PG, alkaline CS, and SS will not only take up large amounts of land but also cause the soil to become salinated and pollute the environment. On the one hand, since the major component of PG is $CaSO_4{\cdot}2H_2O$, numerous researchers have exploited it as a sulfate activator in the preparation of supplemental cementitious materials using possibly water-hardened industrial solid wastes. It has been shown that adding PG can accelerate the dissolution of Ca^{2+}, Al^{3+}, and Si^{4+} in industrial solid wastes, promoting hydrolysis and the formation of more hydrated (aluminium) calcium silicate gels (C-(A)-S-H) and ettringite (AFt), which can improve the strength of SWBCM (Zhao et al., 2021; Yang et al., 2022; Kong et al., 2023; Zhang et al., 2023). On the other hand, the strength of SWBCM may also be increased by SS and CS. Based on the alkalinity of SS and CS, some scholars have used SS and CS as solid waste alkali activators to produce SWBCM. Zhou et al. studied the hydration-hardening properties of a steel slag-red mud-cement-based composite mortar and discovered that the single doping of SS impeded the composite's hydration process in contrast to cement, which reduced the composite's early strength (Zhou et al., 2023). Huang et al. discovered that a reasonable quantity of SS may be employed as an alkali-activator to enhance the activity of GGBS, although the influence on its early excitation is low and the excitation effect occurs mostly late in the hydration process (Huang and Lin, 2010). Wang et al. used high-iron steel slag as an alkali-activator to study the effect on the coagulation and hardening of perovskite phosphogypsum slag cementitious materials, and the results showed that, compared to CaO, high-iron steel slag is not favorable to early slurry strength development, but it has a positive effect on later strength development (Wang et al., 2023b). The above studies show that the stimulatory effect of SS on SWBCM occurs mainly in the later stages. Wang et al. prepared cementitious materials for the cure of marina silty soils via CS to induce SS and GGBS. The results suggested that adding 6% (mass fraction) CS promoted the early strength of silty soils significantly (Wang et al., 2022d). According to Yang et al., CS may significantly improve a wet ground granulated blast furnace slag system's early strength (Yang et al., 2022). An et al. also used CS as an alkali-activator to activate GGBS to prepare GGBS-CS base polymers, and the results showed that adding CS could provide a highly alkaline environment for the dissolution of GGBS particles and improve the rate of the hydration reaction, but too much doping will result in a reduction in the matrix's late strength (An et al., 2023). This suggests that CS has a beneficial stimulation impact on the early hydration of SWBCM, but it needs

10.3389/fmats.2024.1353004

TABLE 1 Chemical compositions of CS, SS, PG, and GGBS (wt%).

Materials	CaO	SiO_2	Al_2O_3	SO_3	Fe_2O_3	K_2O	TiO_2	Na_2O	MgO	P_2O_5	MnO	Other
CS	92.33	3.61	1.93	1.02	0.62	0.05	0.16	–	0.13	0.02	–	0.13
SS	36.71	17.42	6.06	0.60	26.78	0.18	1.34	0.33	4.82	0.53	3.52	1.71
GGBS	40.96	31.55	13.00	2.27	0.36	0.61	1.13	0.51	8.99	0.04	0.38	0.20
PG	37.88	10.54	0.45	49.97	0.18	0.13	0.13	–	–	0.12	–	0.60

to control the dosage reasonably. In summary, SS and CS can be used as alkali activators for SWBCM alone, but there is a problem of insufficient strength of SWBCM at an early or late stage when they are used as alkali activators alone. In addition, most researchers have focused on the effects of SS and CS alone as alkali activators on the mechanical properties and mechanism of action of SWBCM, while studies on the effects of water resistance and the synergistic use of the two as SWBCM alkali activators have been scarcely reported.

In summary, there have been many studies on the preparation of SWBCM from industrial solid wastes as raw materials, but there have been relatively few studies on the synergistic preparation of SWBCM from CS, SS, GGBS, and PG as raw materials, as well as the synergistic use of both CS and SS as alkali activators for SWBCM. In order to improve the early strength of SWBCM while maintaining its late strength and water resistance, based on the respective chemical properties of CS, SS, PG, and GGBS, in this paper, CS-SS-GGBS-PG was prepared by using GGBS as the main material, PG as the sulfate activator, and CS and SS synergistically used as the solid waste alkali activators. The effects of the amount of CS replacing SS (mass fraction) on the flowability, mechanical properties, softening coefficient (K), pore solution pH value, hydration heat, and microstructure of CS-SS-GGBS-PG were investigated. In the meantime, the hydration products have been studied using XRD, FTIR, TG-DTG, SEM, and MIP to identify changes in composition, micromorphology, and pore structure. The results of the study increase SWBCM's use of industrial solid wastes like CS and SS while also lowering SWBCM's dependency on conventional high-angstrom chemical alkali activators, which is significant for both resource conservation and environmental protection.

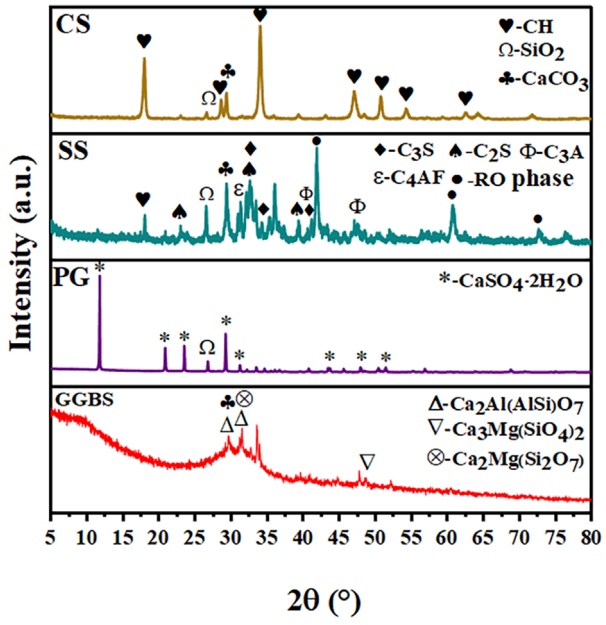

FIGURE 1
XRD patterns of CS, SS, PG, and GGBS.

2 Materials and methods

2.1 Raw materials

The raw materials included CS, SS, PG, and GGBS. CS was obtained from the Hunan Taoyuan acetylene Factory. SS was taken from Kunming City, Yunnan Province, and milled for 60 min using the SM 500 × 500 cement test mill (Cangzhou, China) prior to testing. PG was obtained from Qujing City, Yunnan Province, and before the test, PG was dried in an oven at 50°C until a constant weight and then milled for 30 min using a SM 500 × 500 cement test mill. GGBS was obtained from Qujing, Yunnan Province. The chemical composition of the raw materials was determined using X-ray fluorescence (XRF) (Panalytical Zetium, Netherlands), and the results are reported in Table 1. The mineral composition of the raw materials was determined using an X-ray diffractometer (XRD) (Rigaku SmartLab SE, Tokyo, Japan), and the results are shown in Figure 1. When the results of the XRF and XRD investigations are combined, it is clear that the major chemical composition of CS is CaO, and the main mineral component is CH, which can provide adequate calcium components and an alkaline environment to enhance the system's hydration process. The chemical composition of SS includes CaO, SiO_2, Al_2O_3, Fe_2O_3, etc. The mineral composition is similar to that of ordinary silicate cement, which consists mainly of C_2S, C_3S, C_3A, C_4AF, and RO phases, which are potentially water-hardened and can provide an alkaline environment for the system. The mineral composition of PG is mainly $CaSO_4·2H_2O$, and it contains a large amount of SO_4^{2-}. It can be used as a sulfate activator for the system. The chemical

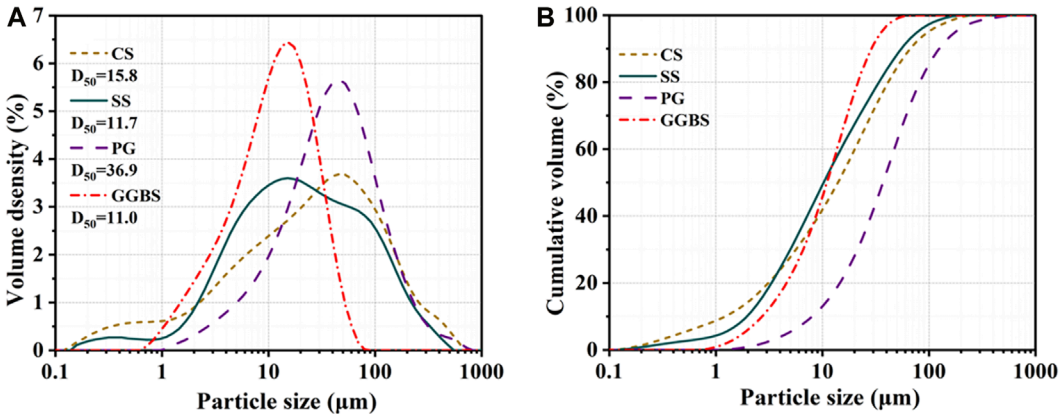

FIGURE 2
Distribution of CS, SS, PG, and GGBS particle sizes (**(A)**: volume density; **(B)**: cumulative volume).

composition of GGBS includes CaO, Al_2O_3, SiO_2, and MgO. GGBS showed no obvious diffraction peaks in XRD (Figure 1), which indicates that GGBS is characterized by an amorphous structure, mainly consisting of amorphous phases such as calcium-aluminium xanthite, magnesium xanthite, and magnesium peridotite, and it has high volcanic ash activity.

Figure 2 displays the particle size distributions of CS, SS, PG, and GGBS according to a Mastersizer 2000 laser particle size analyzer (London, UK). The average particle size (D_{50}) of CS, SS, PG, and GGBS, respectively, were 15.8, 11.7, 36.9, and 11.0 μm.

2.2 Mixture proportion and preparation of samples

The fits used to investigate the effect of the CS replacement rate of SS on the properties and microstructure of CS-SS-GGBS-PG are shown in Table 2, with reference to Zhao et al. (Zhao et al., 2023), who fixed GGBS:SS = 3:1 and PG doping of 20% (Zhu et al., 2023), utilizing 5%, 10%, 15%, and 20% of CS to replace SS, respectively. In order to exclude the effect of water consumption as a parameter on the performance of CS-SS-GGBS-PG, a commonly used value of water-to-binder ratio was chosen in this study, and the water-to-binder ratio was 0.5 for all specimen groups (W/B = 0.5). Weigh each raw ingredient in the ratio shown in Table 2, then add it to the wet-ted cement clean slurry mixer and mix for 2 min on low speed. After that, stop the machine, wait 15 s, and then mix it for 2 min on high speed. Finally, pour the resultant slurry into the vibration molding molds, which measure 40 × 40 × 160 mm and 20 × 20 × 20 mm, respectively. The 40 × 40 × 160 mm specimens were used to test the mechanical properties and K, and the 20 × 20 × 20 mm specimens were used for microtesting. The demolded specimens were sealed with cling film and cured to various ages for performance testing and microtesting at temperatures (20°C ± 2°C) and humidity (>90%). The sample preparation and testing procedures are shown in Figure 3.

TABLE 2 Mixture proportions of specimens (wt%).

Samples	CS/%	SS/%	GGBS/%	PG/%	W/B
A0	0	20	60	20	0.5
A1	5	15	60	20	0.5
A2	10	10	60	20	0.5
A3	15	5	60	20	0.5
A4	20	0	60	20	0.5

2.3 Test methods

2.3.1 Flowability

The effect of the amount of CS-displaced SS on the flowability of CS-SS-GGBS-PG was tested according to the Chinese standard (GB/T 8077–2012). The results were averaged from three parallel tests.

2.3.2 Mechanical properties test

According to the Chinese standard (GB/T 2021), the flexural strength of cementitious sand was tested using a cementitious sand flexural tester (Model DKZ-6000, Wuxi Jianyi Instrument Machinery Co., Ltd., Wuxi City, China), and the results were the average of three parallel tests. The compressive strength was tested using an electro-hydraulic pressure tester (YAW-300B, Jinan Shijin Group Co., Ltd., Jinan City, China), and the results were the average of six parallel tests.

2.3.3 Softening coefficient

After 28 days of sample curing, two sets of samples were taken out and placed in a blast drying oven, drying at a temperature of

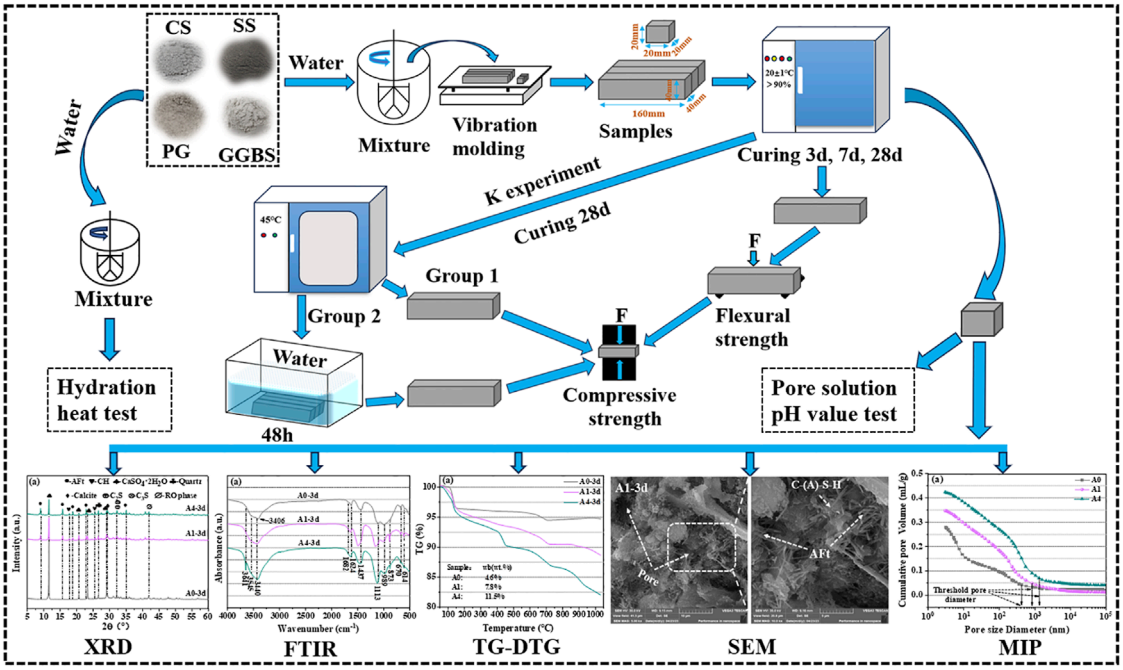

FIGURE 3
Flow chart of preparation and testing of samples.

45°C until a constant mass was achieved. From the dried samples, one set was selected for compressive strength (f) testing. The other set of samples was immersed in water for 48 h, then taken out and tested for compressive strength (F). The softening coefficient is characterized by K = F/f.

2.3.4 Pore solution pH value test

In order to investigate the influence of the amount of CS replacing SS on the pore solution pH values in the CS-SS-GGBS-PG system at different maintenance ages, 5 g of sample powder from various age periods were added to 50 g of deionized water. The mixture was stirred at a speed of 180 revolutions per minute for 30 min. Subsequently, the solution was filtered, and the pH value was measured using a pH meter (Sigma pH838), with an accuracy of 0.01.

2.3.5 Hydration heat test

Hydration heat testing of CS-SS-GGBS-PG was performed using the TAM Air eight isothermal calorimeter. The slurry was thoroughly mixed externally, weighed, transferred into glass ampoules, and immediately placed into the calorimeter for measurement.

2.4 Methods of characterization

2.4.1 XRD

The hydration products of CS-SS-GGBS-PG were characterized by XRD (same model as in Section 2.1). The scanning range was 5°–60°, and the scanning speed was 2°/min.

2.4.2 FTIR

The specimens were combined in a 1:100 ratio with potassium bromide and formed into tablets. A Thermo Scientific iN10 infrared spectrometer (Waltham, MA, United States) was used to examine the hydration products. The scanning range was 500–4,000 cm^{-1} (Mi et al., 2023).

2.4.3 TG-DTG

The TG-DTG analysis was carried out on a STA8000 calorimeter (PerkinElmer, Waltham, MA, United States) with a temperature range of 50°C–1,050°C and a heating rate of 15°C/min.

2.4.4 SEM

The samples' micro-morphology was examined using a VEGA3LMU high-and low-variable vacuum tungsten scanning electron microscope.

2.4.5 MIP

The pore structure of CS-SS-GGBS-PG was analyzed using a high-performance fully automated mercuric piezometer (Micromeritics Auto Pore IV 9510, Norcross, GA, United States) with pore sizes ranging from 3 to 1 mm and pressure ranging from 0.10 to 60,000.00 psia.

3 Results and discussion

3.1 Effect of the amount of CS substituted for SS on the flowability of CS-SS-GGBS-PG

The results of the effect of the amount of CS substituted with SS on the flowability of CS-SS-GGBS-PG are shown in Figure 4. It

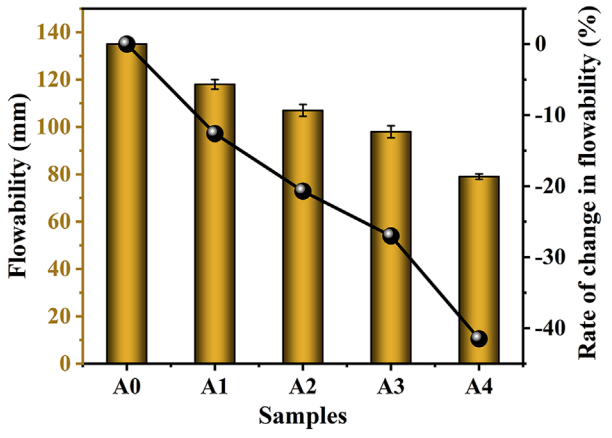

FIGURE 4
Effect of the amount of CS substituted for SS on the flowability of CS-SS-GGBS-PG.

can be seen that the flowability of the freshly mixed slurry of CS-SS-GGBS-PG shows a decreasing trend with the increasing amount of CS substituted for SS. The value for A0 is 135 mm, while the values for A1, A2, A3, and A4 are 118, 107, 98, and 79 mm, respectively, which are 12.6%, 20.7%, 27%, and 41.5% lower than that for A0, respectively. On the one hand, the main chemical component of CS is CaO, and the addition of CS brings a large amount of CaO to the system. CaO dissolved in water creates an exothermic reaction, and the heat created by the reaction process consumes the system's water, increasing the water need of the newly mixed slurry. On the other hand, it can be seen from Figure 2 that the cumulative volume of CS below 4 μm is larger than that of SS, and smaller particle size powders adsorb more water, which makes CS substitute for SS to increase the amount of water required for CS-SS-GGBS-PG. The above two reasons lead to a decrease in the flowability of CS-SS-GGBS-PG with an increase in the amount of CS displacing SS at the same water-to-binder ratio.

3.2 Effect of the amount of CS substituted for SS on the mechanical properties of CS-SS-GGBS-PG

Figure 5 depicts the influence of the quantity of CS substitution SS on the mechanical properties of CS-SS-GGBS-PG. It can be observed that A0 exhibits lower early strength, with flexural and compressive strengths reaching only 0.1 MPa after 3 days of curing. This is mostly due to the system's low alkalinity, which does not assist the hydration of the active component in the GGBS efficiently, resulting in fewer hydration products and, thus, poor flexural and compressive strengths (Ma et al., 2022). When compared to A0, the 3 days lexural and compressive strengths of the specimen containing CS grew significantly as the quantity of CS replaced SS. At 3 days of curing, the flexural strengths of A1, A2, A3, and A4 were 0.5 MPa, 0.8 MPa, 1.0 MPa, and 1.2 MPa, respectively, which increased by 400%, 700%, 900%, and 1,100%, respectively, compared to A0 (Figure 5C). The compressive strengths were 0.9 MPa, 1.7 MPa, 2.2 MPa, and 2.6 MPa, which were 800%, 1,600%, 2,100%, and 2,500% higher than those for A0, respectively (Figure 5D). This was attributed to the fact that the addition of CS eliminated the unfavorable effects of partially soluble phosphorus and fluorine in PG (Wang, 2021) and, at the same time, increased the alkalinity level of the CS-SS-GGBS-PG system, which facilitated the breakage of the Ca-O, Si-O-Al, and O-Si-O bonds in the GGBS particles (Song and Jennings, 1999; Wang et al., 2022a), and accelerated the formation of the C-(A)-S-H gels and the AFt in the system, which improved the early strength of the CS-SS-GGBS-PG. At 7 days of curing, the strength of CS-SS-GGBS-PG still increased with the increase in the amount of CS replacing SS, but the increase was smaller when the amount of CS replacing SS exceeded 5%, which indicated that the effect was not more pronounced with the increase in the amount of CS replacing SS. It is also noteworthy that the 28 days strength of CS-SS-GGBS-PG decreased as the amount of CS substitution increased. It can be seen that the replacement of SS by CS increased the concentrations of Ca^{2+} and OH^- in the CS-SS-GGBS-PG system, thus promoting the early hydration reaction. However, at too high a concentration of OH^-, OH^- reacts preferentially with Ca^{2+} to form CH rather than participating in the polymerization reaction to generate C-S-H gels (Wang et al., 2022e), which may lead to the inhibition of the generation of C-S-H gels. Therefore, when the amount of CS-displaced SS exceeded 5%, the 7 days strength of CS-SS-GGBS-PG did not significantly increase with the increase of CS-displaced SS. It is also noteworthy that the 28 days strength of CS-SS-GGBS-PG decreased with the increase in the CS replacement SS amount. In summary, the substitution of SS with CS can significantly enhance the early strength of CS-SS-GGBS-PG. However, an excessive replacement may lead to a reduction in the later-stage strength of CS-SS-GGBS-PG. The appropriate replacement ratio for CS should be controlled around 5%.

Furthermore, the flexural strength of the CS-SS-GGBS-PG specimen groups with varying percentages of CS replaced for SS changed less than the compressive strength at all ages, as seen in Figures 5C, D. In comparison to the flexural strength, it shows that the substitution of SS with CS has a considerable impact on the compressive strength of CS-SS-GGBS-PG.

It has been shown that the compressive and flexural strengths of cementitious materials have a strong linear relationship (Wu et al., 2018). Figure 6 depicts the relationship between compressive strength and flexural strength of CS-SS-GGBS-PG, showing a clear linear correlation (R^2 = 0.91175) between them. It implies that the equations in the picture accurately depict the connection between this material's compressive and flexural strength.

3.3 Effect of the amount of CS substituted for SS on the softening coefficient of CS-SS-GGBS-PG

K is an index that characterizes the water resistance of a material, and a K value greater than 0.85 is considered to indicate a water-resistant material (Guo, 2020). As shown in Figure 7, the K value of CS-SS-GGBS-PG decreases as the quantity of CS replaced for SS grows, which is consistent with the trend of CS-SS-GGBS-PG strength. In particular, when the amount of CS substitution exceeded 5%, the K value of CS-SS-GGBS-PG decreased sharply with the

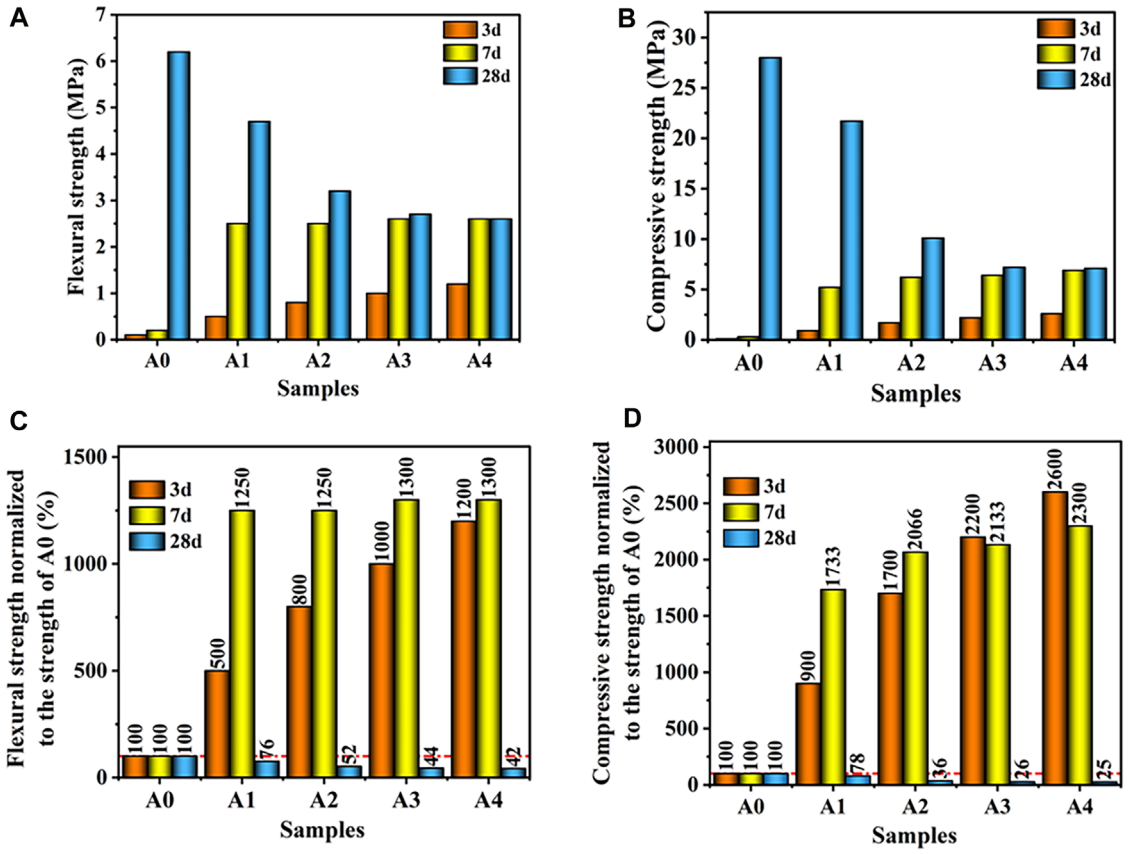

FIGURE 5
Effect of the amount of CS substituted for SS on the mechanical properties of CS-SS-GGBS-PG ((**A**): flexural strength; **(B)**: compressive strength; **(C)**: normalized flexural strength to A0 strength; **(D)**: normalized compressive strength to A0 strength).

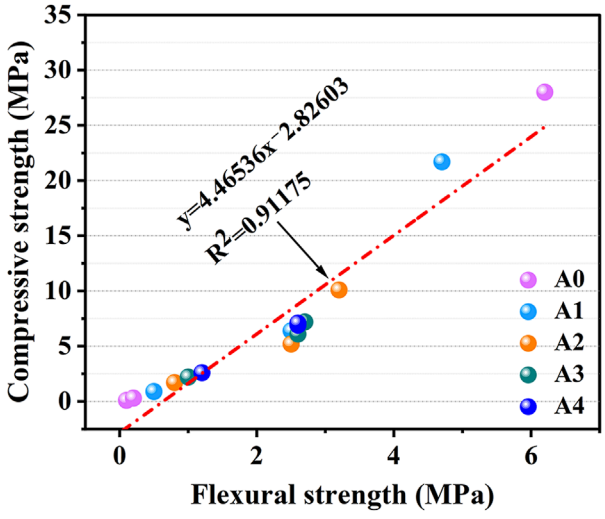

FIGURE 6
The relationship between the compressive and flexural strengths of CS-SS-GGBS-PG.

increase in the amount of CS substitution for SS, and all of the values were less than 0.85, showing poor water resistance. The reason for this is that the increase in the amount of CS displacing SS after 28 days of hydration results in a substantial presence of CH and a significant amount of unconsumed PG in the CS-SS-GGBS-PG system. This observation can be discerned from the results of the tests in Section 2.4 (XRD, FTIR, TG-DTG). The presence of a large amount of CH makes the system unstable (Wan et al., 2022), and CH dissolves when it comes into contact with water, destroying the microstructure of the sample (Guo, 2020) and thus reducing the strength of CS-SS-GGBS-PG. Additionally, after water absorption, the strength of the unreacted PG reduced, resulting in a drop in the strength of CS-SS-GGBS-PG in the water-saturated state, which resulted in a decrease in the K value.

3.4 Effect of the amount of CS substituted for SS on the pore solution pH value of CS-SS-GGBS-PG

The research indicates that the dissolution extent of GGBS is largely dependent on the pH exhibiting its activity only when the

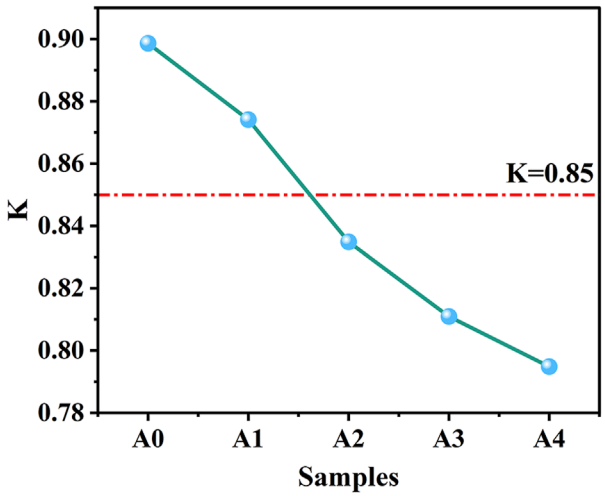

FIGURE 7
Effect of the amount of CS substituted for SS on the softening coefficient of CS-SS-GGBS-PG.

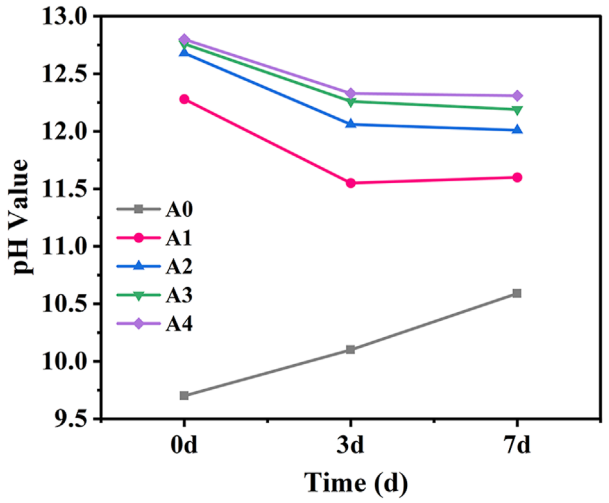

FIGURE 8
Effect of the amount of CS substituted for SS on the pore solution pH value of CS-SS-GGBS-PG.

pH exceeds 11.5 (Chen et al., 2023). Figure 8 illustrates the impact of varying levels of CS substitution for SS on the pH values of the pore solution of CS-SS-GGBS-PG at the initial state, 3, and 7 days of curing. It can be observed that the pH values of the pore solution at the initial state, 3 and 7 days increase with the higher substitution of CS for SS in CS-SS-GGBS-PG, consistent with the results of the mechanical strength tests. The pore solution pH values of the A0 sample increase with the duration of curing, attributed to the hydration of silicate minerals in SS forming CH. However, the pore solution pH values of A0 at the initial, 3 and 7 days stages are significantly lower than those of other sample groups, all below 11.5, indicating lower alkalinity. Nevertheless, this lower alkalinity is insufficient to break down the glassy phase in GGBS, preventing the effective dissolution of reactive silica-alumina into the pore solution for hydration reactions. This is the primary reason for the significantly lower early strength of the A0 sample compared to other groups. The pore solution pH values of A1 exhibit a trend of initially decreasing and then slightly increasing with the duration of curing. The sharp decrease in pore solution pH values during the first 3 days is attributed to the consumption of CH, a hydration product of CS. While, the slight increase in pore solution pH values from 3 to 7 days may be related to the generation of CH by SS hydration. As a result, the pore solution pH values exhibit a pattern of initially decreasing and then slightly increasing with the duration of curing. Furthermore, the pore solution pH values of A2, A3 and A4 decrease with the duration of curing, attributed to the consumption of CH during the hydration reaction.

3.5 Hydration heat evolution

Figure 9A displays the hydration heat release rate curves within 168 h for CS-SS-GGBS-PG under different levels of CS substitution for SS. From Figure 9A, it can be observed that CS-SS-PG-GGBS exhibits two primary exothermic peaks. The first exothermic peak occurs within the first hour of CS-SS-PG-GGBS coming into contact with water, attributed to the dissolution of various mineral phases in the raw materials. The second exothermic peak appears after 10 h, and with an increasing substitution of CS for SS, this peak becomes more pronounced, exhibiting a longer duration of exothermic activity. Within 168 h, the A0 sample does not show a distinct second exothermic peak, whereas the samples with added CS clearly exhibit this peak. Moreover, as the amount of CS substitution for SS increases, the induction period of this peak shortens, and the peak value rises. This can be attributed to two main factors: first, the exothermic reaction involving CaO dissolution in water to form CH within CS, and second, the volcanic ash reaction between GGBS and CH (Zhao et al., 2023).

Figure 9B illustrates the cumulative heat release curves within 168 h for CS-SS-GGBS-PG under different levels of CS substitution for SS. The cumulative heat release for A0 within 168 h is only 5.6 J/g, while for A1, A2, A3, and A4, it is 102.2, 124.4, 120.0, and 121.2 J/g, respectively. It is evident that the addition of CS significantly enhances the total hydration heat of CS-SS-GGBS-PG. The hydration heat results indicate that CS markedly increases the heat release rate and overall hydration heat of CS-SS-GGBS-PG.

3.6 Micro-analysis

3.6.1 XRD analysis

Figure 10 shows the results of an XRD examination performed on A0, A1, and A4 after 3 and 28 days of curing. The crystalline phases of the CS-SS-GGBS-PG hardened slurry are more complex, mainly AFt, $CaSO_4{\cdot}2H_2O$, CH, C-(A)-S-H gels, calcium silicate (C_2S, C_3S), quartz (SiO_2), calcite ($CaCO_3$), and the RO phase. Among them, CH, AFt, and C-(A)-S-H gels are newly produced hydration products during the hydration process, while C_2S, C_3S, SiO_2, $CaCO_3$, $CaSO_4{\cdot}2H_2O$, and RO phases can be found in the raw material. Moreover, $CaCO_3$ is linked to the carbonation of

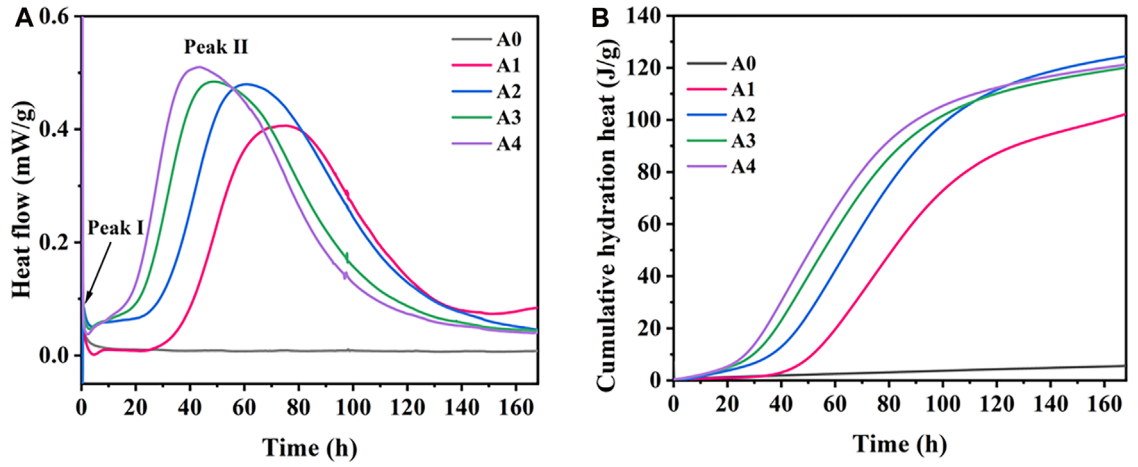

FIGURE 9
Hydration heat of CS-SS-GGBS-PG ((**A**): heat flow; (**B**): cumulative hydration heat).

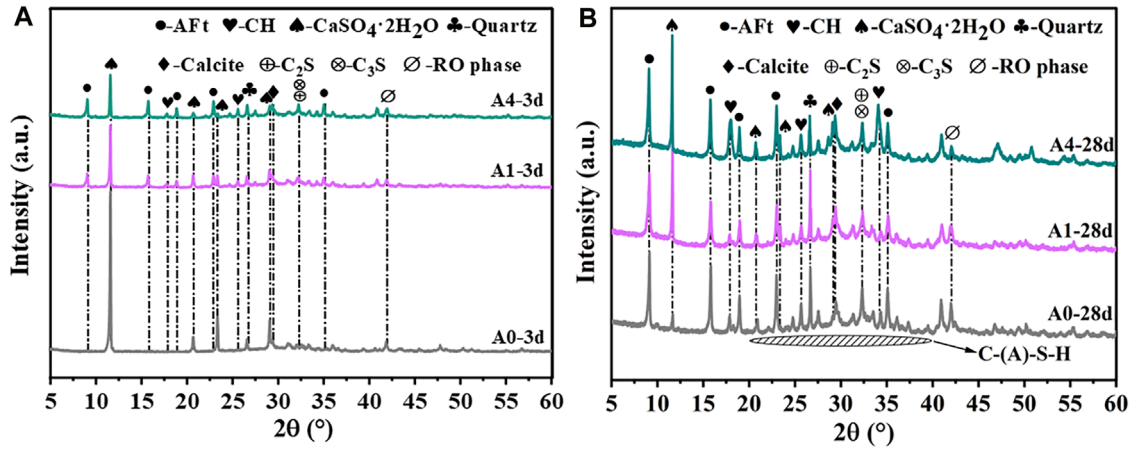

FIGURE 10
XRD pattern of CS-SS-GGBS-PG ((**A**): A0, A1, and A4 curing 3d; (**B**): A0, A1, and A4 curing 28d).

C-S-H gels during sample curing (Huo et al., 2021). Due to the amorphous nature of C-(A)-S-H gels, which corresponds to a broad diffused peak in the range of 20°–40° in the XRD spectrum, there are no distinct diffraction peaks observed in the XRD pattern (Ma et al., 2023).

Figure 10A makes it evident that after 3 days of curing, no discernible new diffraction peaks developed in A0, suggesting that the degree of hydration was very low and that hardly any hydration products were produced. In comparison to A0, the strength of the $CaSO_4{\cdot}2H_2O$ diffraction peak in A1 and A4 was much less, and the AFt and CH diffraction peaks were clearly visible. It suggests adding an amount of CS to enhance the system's alkalinity, expedite the consumption of $CaSO_4{\cdot}2H_2O$ in PG, and promote the synthesis of AFt in the system. However, after 28 days of curing (Figure 10B), the diffraction peaks of $CaSO_4{\cdot}2H_2O$ in A1 and A4 were significantly stronger than those of A0, and those of A4 were stronger than those of A1. This suggests that the excessive addition of CS weakens the late hydration reaction of PG with GGBS and SS, resulting in a large amount of unconsumed PG remaining in the system after 28 days of curing, and the unconsumed PG mainly serves as a filler. Since the strength of PG crystals is extremely low, their contribution to the strength of CS-SS-GGBS-PG is minimal when used as an aggregate filler (Ma et al., 2022). Consequently, this leads to a reduction in the strength of CS-SS-GGBS-PG.

3.6.2 FTIR analysis

The results of FTIR examinations at wavelengths of 500 cm^{-1}–4,000 cm^{-1} for cured A0, A1, and A4 for 3 days and 28 days are shown in Figure 11. The FTIR spectra of different samples are highly similar, with essentially the same absorption bands in the spectrum but differing in absorbance levels. The stretching vibration band of Ca-OH in CH is shown by the absorption band at 3,641–3,643 cm^{-1} (Delgado et al., 1996; Ylmén et al., 2009). The high-frequency region's absorption bands at 3,545 and 3,406 cm^{-1} are brought on by the symmetric and asymmetric vibrations of

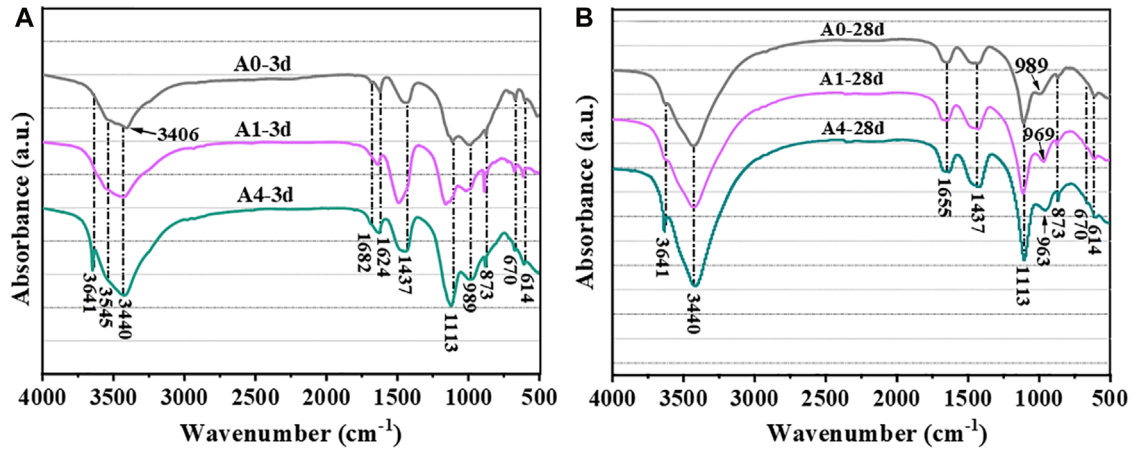

FIGURE 11
FTIR pattern of CS-SS-GGBS-PG ((**A**): A0, A1, and A4 curing 3d; (**B**): A0, A1, and A4 curing 28d).

stretching of H_2O (O-H) in PG (Ylmén et al., 2009; Wang et al., 2022b). The bending vibrational bands of H_2O (O-H) in PG are located at 1,682 and 1,624 cm^{-1} (Ylmén et al., 2009). The absorption band observed near 3,440 cm^{-1} is the stretching vibration band of $[Al(OH)_6]^{3-}$ (Al-OH) in AFt (Zhang et al., 2022; Kong et al., 2023). It indicates that there is AFt generation during hydration. The absorption band at 1,655 cm^{-1} is the bending vibration band of O-H in C-S-H gels (Lin et al., 2021b), and the absorption bands at 600–853 cm^{-1} and 938–997 cm^{-1} correspond to the bending vibration of Al-O-H and the asymmetric stretching vibration of Si-O-Si (Si-O-Al) in the C-(A)-S-H gels, respectively (Ylmén et al., 2009; Lin et al., 2020). It is shown that there is C-(A)-S-H gels generation during hydration. The absorption band located near 1,113 cm^{-1} is associated with SO_4^{2-} in PG (Lan et al., 2022; Wang et al., 2023a). Additionally, the absorption band seen at 1,437 cm^{-1} is an asymmetric stretching vibrational absorption band of CO_3^{2-} (Zhang et al., 2010), while the sharp absorption band seen at 873 cm^{-1} is generated by an out-of-plane bending vibration of CO_3^{2-} (Lin et al., 2021b). The bands that absorb CO_3^{2-} have to do with the carbonate in the test material and the vibration of CO_3^{2-} ions made when the C-S-H gels carbonize during the sample preservation period (Huo et al., 2021; Ma et al., 2023).

From Figure 11A, it can be seen that there are obvious absorption bands at 3,545, 3,406, 1,682 and 1,624 cm^{-1} for A0 at 3 days of curing, whereas the absorption bands of A1 and A4 at this wave number are obviously weakened and the absorption band at 3,440 cm^{-1} is obviously enhanced. It means that the addition of CS reduced the consumption of PG, aided in the production of AFt, and increased the early strength of CS-SS-PG-GGBS. However, after 28 days of curing (Figure 11B), A4 had a substantial absorption band at 3,641 cm^{-1} compared to A0 and A1, showing that there was a large amount of CH in A4 that was not consumed. Besides, the absorption peaks around 1,113 cm^{-1} in A1 and A4 are significantly stronger than in A0, with A4 being stronger than A1, providing additional confirmation that excessive CS substitution for SS weakens the consumption of PG in the later hydration stages, consistent with the XRD test results.

3.6.3 TG-DTG analysis

Figure 12 depicts the TG-DTG curves of A0, A1, and A4 after 3 and 28 days of curing at 50°C–1,050°C. According to previous studies, it is widely believed that the endothermic peak around 100°C is attributed to the dehydration of C-(A)-S-H and AFt (Lin et al., 2021a; Meskini et al., 2021). The large heat absorption peak at 130°C is caused by $CaSO_4{\cdot}2H_2O$ dehydration, which is not involved in the hydration process (Li et al., 2020). The thermal breakdown of CH is responsible for the characteristic peak around 400°C–500°C (Lin et al., 2021b; Xu et al., 2021). Furthermore, the decarbonization of $CaCO_3$ often takes place between 600°C and 900°C, mostly due to the carbonates in the raw material breaking down or the sample being carbonated during the preservation process (Lin et al., 2021b).

The $CaSO_4{\cdot}2H_2O$ heat absorption peak of A1 and A4 was dramatically attenuated compared to that of A0 in the DTG curves of the 3 days of curing samples (Figure 12B), exhibiting that the addition of CS greatly increased the consumption of PG. Further, the development of cementitious material strength is often linearly proportional to the content of chemically bound water (Wb) (Atasoy, 2005), and the content of Wb was estimated for each specimen at various curing ages using the De Weerdt et al. method (De Weerdt et al., 2010), Figures 12A, C illustrate the findings. At 3 days of curing, the Wb values for A0, A1, and A4 are 4.6%, 7.8%, and 11.5%, respectively. It is evident that the addition of CS significantly increases the early hydration degree of CS-SS-GGBS-PG, improving the early strength of the matrix. However, after 28 days of curing, the Wb content of the three specimens was in the order of A4 (20.5%) > A1 (19.6%) > A0 (16.3%), while the compressive strength was in the order of A4 < A1 < A0, with the Wb content of A1 and A4 being much lower than that of A0. The reason for this is that there is more unconsumed CH (Figure 12D) and residual PG in A1 and A4 than in A0, and the microstructural compactness is poorer than in A0 (Sections 3.6.4, 3.6.5), which results in lower strengths of A1 and A4 than in A0. The findings of the TG-DTG tests concur with the findings of the XRD and FTIR tests, demonstrating once more that the early strength development of CS-SS-GGBS-PG is positively

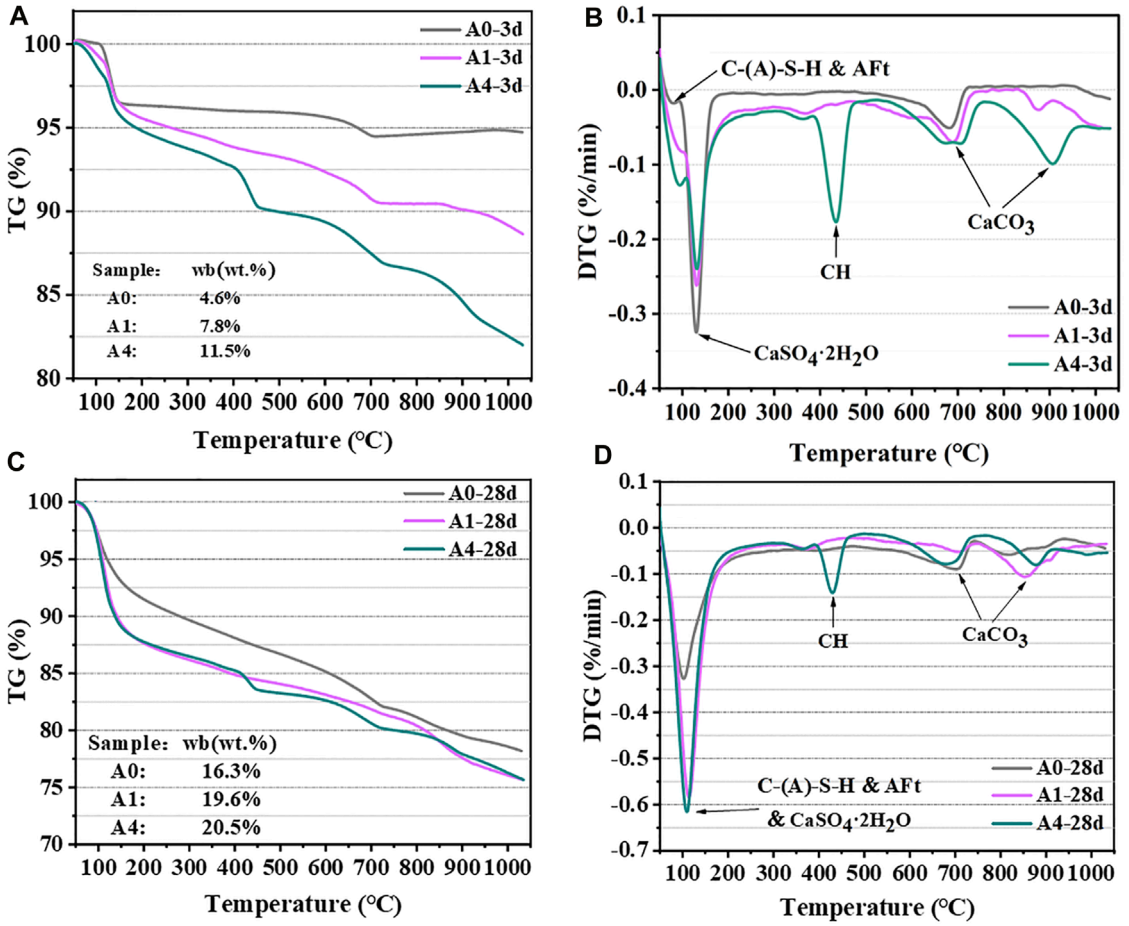

FIGURE 12
TG-DTG results of CS-SS-GGBS-PG (**(A, B)**: A0, A1, and A4 curing 3d; **(C, D)**: A0, A1, and A4 curing 28d).

impacted by the moderate replacement of SS with CS, while the late strength development of CS-SS-GGBS-PG is negatively impacted by excessive substitution.

3.6.4 SEM analysis

As shown in Figure 13, the hydration products of CS-SS-GGBS-PG were characterized by SEM to reveal the microstructure of CS-SS-GGBS-PG. It is evident from the crystal morphology of the hydration products that the hydration products of CS-SS-GGBS-PG are mostly C-(A)-S-H gels that resemble networks and needle-columnar AFt (Hao et al., 2022; Yang et al., 2022). Moreover, in contrast to XRD, FTIR, and TG-DTG results, SEM images did not reveal distinct plate-like $CaSO_4{\cdot}2H_2O$ and flake-like CH. This discrepancy may be attributed to their coverage by AFt and C-(A)-S-H gels.

From the images, it can be observed that AFt and C-(A)-S-H gels are present in all SEM images. However, compared to A0, there are significant changes in the microstructure of A1 and A4 at 28 days. During the 28 days curing period, in the SEM images of A0, a substantial amount of needle-like AFt can be observed. These AFt structures interlace and intertwine with each other, forming a dense configuration that fills the pores. Additionally, they are enveloped by C-(A)-S-H gels, resulting in a relatively compact microstructure. However, compared to A0, the microstructures of A1 and A4 had noticeably larger pores, which led to worse densification. Overall, the specimens containing CS had a lower degree of densification in their microstructure than specimens having A0, and the result was more noticeable the more CS substituted for SS.

3.6.5 MIP analysis

Cementitious materials' mechanical and physical properties are strongly correlated with their pore structure, in addition to being dependent on the quantity of hydration products present. MIP was used to determine the pore structure of A0, A1, and A4 after 28 days of curing, and the results are shown in Figure 14. Table 3 also provides the primary pore structure data for the three specimens, including the total pore volume, porosity, average pore size, threshold pore diameter, and critical pore diameter. Figure 14A shows that the cumulative pore volume grew steadily as pore size decreased, with the ultimate value of the total pore volume being 0.2794 mL/g for A0 and 0.3477 mL/g and 0.4233 mL/g for A1 and A4, which were 24.4% and 51.5% greater than A0, respectively. This shows that an excessive amount of CS replacing SS causes more pores and poorer densification in the microstructure of CS-SS-GGBS-PG. This discovery aligns with the outcomes noted by SEM. The cumulative pore volume profiles of A0, A1, and A4 began

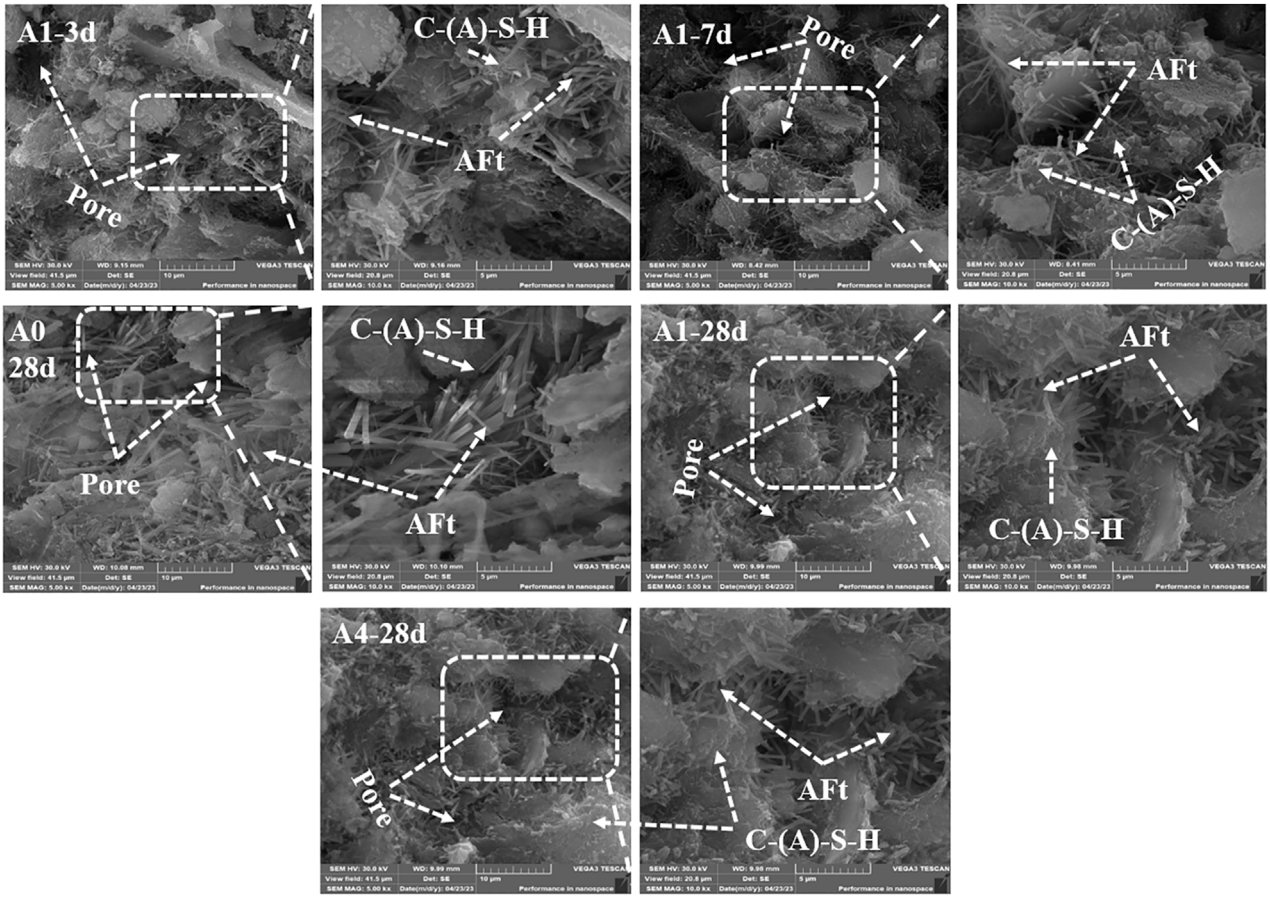

FIGURE 13
SEM images.

to grow significantly at 423.60 nm, 830.57 nm, and 1,313.79 nm, respectively (Figure 14A), and these characteristic pore diameters are referred to as the "threshold pore diameter". Above this aperture, Hg intrusion is negligible, whereas below this aperture, Hg intrusion starts to increase rapidly (Jang and Lee, 2016; Song et al., 2020). Furthermore, the wave peaks in the incremental pore volume curves correspond to the critical pore diameter (Liu et al., 2019), which was 6.03 nm, 226.98 nm, and 422.48 nm for A0, A1, and A4, respectively (Figure 14B). The critical pore diameters of A1 and A4 were considerably pushed towards a large pore size in comparison to A0, suggesting that the substitution of CS for SS increased the quantity of massive pores in the matrix. Research indicates that the threshold pore diameter and average pore size of the composite cementitious material increase with increasing critical pore diameter (Liu et al., 2019), and the test findings of this investigation support this conclusion (Table 3).

Generally speaking, the lower a composite's porosity, the higher its strength; also, the average pore size is an essential indication of pore structure; in general, the smaller the average pore size, the denser the microstructure of the composite material, and the higher the strength (Liu et al., 2019). According to Table 3, the porosity and average pore diameter of CS-SS-GGBS-PG increase with the increase in CS substitution for SS. This indicates that excessive CS-substituted SS will adversely affect the pore structure of CS-SS-GGBS-PG, leading to a reduction in matrix strength.

To further quantitatively investigate the impact of CS substitution for SS on the pore distribution of CS-SS-GGBS-PG, based on previous studies, the pores in the CS-SS-GGBS-PG system were classified into four groups, including small gel pores (<10 nm), large gel pores (10nm–50 nm), capillary pores (50nm–100 nm), and large pores (>100 nm) (Ma et al., 2013; Keulen et al., 2018; Song et al., 2020). The volume fractions of each group of pores are shown in Figure 14C. Gel pores, also known as harmless pores or micropores, are formed by the production of C-(A)-S-H gels (Chuah et al., 2016). They have an effect on drying shrinkage, creep, and microstructure (Peng, 2013; Liu and Wang, 2018). Harmful pores are those that are bigger than 50 nm and have a greater impact on the composite's strength and permeability (Hao et al., 2022). Figure 14C shows that the gel pores of A0 had the highest pore volume fraction (59.1%), whereas the gel pores of A1 and A4 had higher hazardous pore volume percentages of 63.5% and 71.8%, respectively. This was because the addition of CS weakened the reaction system's late hydration reaction (XRD, FTIR, and TG-

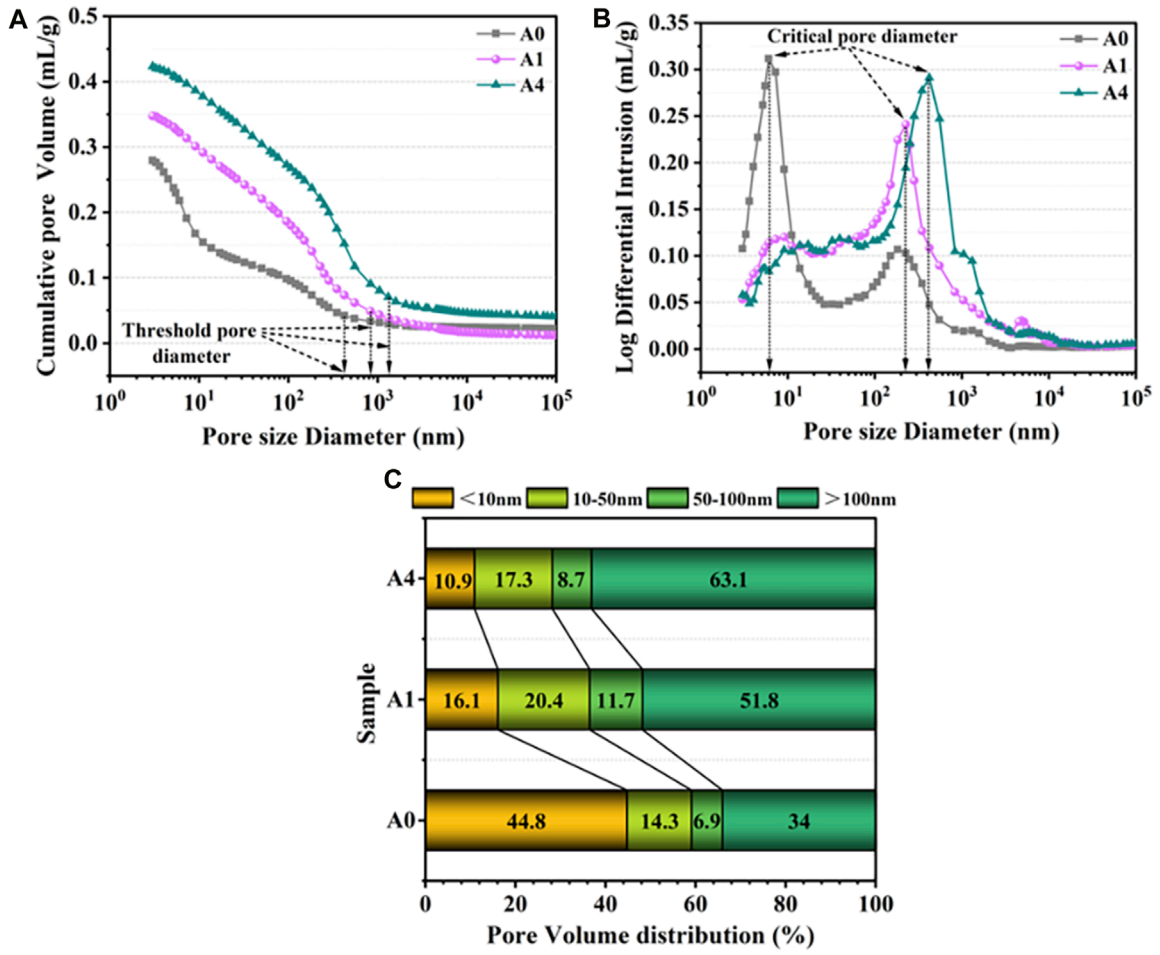

FIGURE 14
Pore structure characteristics ((**A**) cumulative pore volume; (**B**) Log differential intrusion; (**C**) pore volume fraction) for A0, A1 and, A4 curing for 28d.

TABLE 3 Main pore structure parameters for A0, A1, and A4.

Samples	Total pore volume (mL/g)	Threshold pore diameter (nm)	Critical pore diameter (nm)	Average pore diameter (nm)	Porosity (%)
A0	0.2794	423.6	6.03	11.32	38.65
A1	0.3477	830.57	226.98	24.93	45.10
A4	0.4233	1,313.79	422.48	34.48	49.57

DTG results), resulting in fewer hydrated gel products, and the harmful pores could not be well filled, resulting in poorer densification of the microstructures and a reduction in the strength of CS-SS-GGBS-PG.

4 Conclusion

In this study, CS-SS-GGBS-PG was prepared from industrial solid wastes, with GGBS as the main material, CS and SS as alkali

activators, and PG as a sulfate activator. Studied the influence of the quantity of CS substitution for SS on the macroscopic properties and microstructure of CS-SS-GGBS-PG. The following are the conclusions.

1. Compared to the specimen without CS (A0), the flowability of CS-SS-GGBS-PG is reduced when SS is substituted with CS. The addition of CS provides a highly alkaline environment and sufficient calcium components for the CS-SS-GGBS-PG system, accelerating the progress of hydration reactions and significantly enhancing the early strength of CS-SS-GGBS-PG. Compared to A0, samples with 5% CS-displaced SS showed 400% and 1,150% increases in flexural strength at 3 and 7 days, respectively, and 800% and 1,633% increases in compressive strength, respectively. However, too much replenishment decreases its 28 days strength. It is advised that the SS-to-CS mixing ratio be 3:1 in order to boost the early strength of CS-SS-GGBS-PG while avoiding the unfavorable impact of too high a replacement on the later strength.
2. When the quantity of CS substituted for SS increased, the K of CS-SS-GGBS-PG exhibited a downward trend. When the amount of CS substituted for SS was more than 5%, the K values all abruptly declined and were less than 0.85, indicating poor water resistance.
3. The microtest findings demonstrate that CS may replace SS in the early stages of CS-SS-GGBS-PG by causing the formation of additional C-(A)-S-H gels and AFt, which helps to increase the CS-SS-GGBS-PG early strength. Excessive substitution, however, will weaken the system's late hydration reaction, resulting in an increase in CH and PG in the system, which are not involved in the hydration reaction after 28 days of hydration, resulting in an increase in harmful pores in the specimen's microstructure and a deterioration in the degree of compactness.
4. This study has a good impact on the combined use of SS and SS as well as the creation of SWBCM. If the region has a large amount of unutilized CS and SS, they can be used to synergistically stimulate potentially water-hard industrial solid waste in appropriate proportions and supplement it with an appropriate amount of PG to prepare SWBCM to replace part of the cement in applications with relatively low strength requirements, such as road bedding, mine backfilling, and so on. This may help increase the use of industrial solid waste and significantly lower the cement industry's carbon footprint.

Data availability statement

The original contributions presented in the study are included in the article/Supplementary material, further inquiries can be directed to the corresponding author.

Author contributions

GY: Writing–original draft, Conceptualization. CL: Writing–review and editing, Resources, Project administration. WX: Writing–review and editing, Funding acquisition. YY: Writing–review and editing, Supervision, Investigation. CK: Writing–review and editing, Data curation. XL: Writing–review and editing, Validation.

Funding

The author(s) declare financial support was received for the research, authorship, and/or publication of this article. This study was supported by "Technological Innovation and Demonstration Project of Departement of Transport of Yunnan Province (No. Yjkb[2021] No. 39); Yunnan Major Scientific and Technological Projects (grant No. 202202AG050020)."

Conflict of interest

Author GY was employed by China Railway Construction Kunlun Investment Group Co., Ltd. Authors CL and WX were employed by China Railway Construction Yunnan Investment Co., Ltd.

The remaining authors declare that the research was conducted in the absence of any commercial or financial relationships that could be construed as a potential conflict of interest.

Publisher's note

All claims expressed in this article are solely those of the authors and do not necessarily represent those of their affiliated organizations, or those of the publisher, the editors and the reviewers. Any product that may be evaluated in this article, or claim that may be made by its manufacturer, is not guaranteed or endorsed by the publisher.

References

An, S., Wang, B. M., Chen, W. X., and Wang, X. J. (2023). Performance and action mechanism of slag–carbide slag based geopolymer. *Bull. Chin.Ceram. Soc.* 42, 3996–4005. doi:10.16552/j.cnki.issn1001-1625.20230928.002

Atasoy, A. (2005). An investigation on characterization and thermal analysis of the Aughinish red mud. *J. Therm. Anal. Calorim.* 81, 357–361. doi:10.1007/s10973-005-0792-5

Chen, Y. Z., Wu, X. Q., Yin, W. S., Li, W. M., and Tang, S. C. (2023). Effect of calcium carbide residue on mechanical properties and microstructure of composite cementitious material. *Bull. Chin.Ceram. Soc.* 42 (09), 3196–3203. doi:10.16552/j.cnki.issn1001-1625.2023.09.025

Chuah, S., Duan, W. H., Pan, Z., Hunter, E., Korayem, A. H., Zhao, X. L., et al. (2016). The properties of fly ash based geopolymer mortars made with dune sand. *Mater. Des.* 92, 571–578. doi:10.1016/j.matdes.2015.12.070

Delgado, A. H., Paroli, R. M., and Beaudoin, J. J. (1996). Comparison of IR techniques for the characterization of construction cement minerals and hydrated products. *Appl. Spectrosc.* 50, 970–976. doi:10.1366/0003702963905312

De Weerdt, K., Haha, M. B., Le Saout, G., Kjellsen, K. O., Justnes, H., and Lothenbach, B. (2010). Hydration mechanisms of ternary Portland cements containing limestone powder and fly ash. *Cem. Concr. Res.* 41, 279–291. doi:10.1016/j.cemconres.2010.11.014

GB/T (2021). *Test method of cement mortar strength (ISO Method)*. Beijing, China: China Standards Press.

GB/T 8077–2012 (2012). *Methods for testing uniformity of concrete admixture*. Beijing, China: China Standards Press.

Guo, X. Y. (2020). *Study on binding properties of modified slag cement in preparation of both sintering-free bricks of respective muck and phosphogypsum*. Beijing: Anhui University of Technology.

Hao, X. S., Liu, X. M., Zhang, Z. Q., Zhang, W., Lu, Y., Wang, Y. G., et al. (2022). In-depth insight into the cementitious synergistic effect of steel slag and red mud on the properties of composite cementitious materials. *J. Build. Eng.* 52, 104449. doi:10.1016/j.jobe.2022.104449

Huang, Y., and Lin, Z. S. (2010). Investigation on phosphogypsum–steel slag–granulated blast-furnace slag–limestone cement. *Constr. Build. Mater.* 24, 1296–1301. doi:10.1016/j.conbuildmat.2009.12.006

Huo, B. B., Li, B. L., Chen, C., and Zhang, Y. M. (2021). Surface etching and early age hydration mechanisms of steel slag powder with formic acid. *Constr. Build. Mater.* 280, 122500. doi:10.1016/j.conbuildmat.2021.122500

Jang, J. G., and Lee, H. K. (2016). Effect of fly ash characteristics on delayed high-strength development of geopolymers. *Constr. Build. Mater.* 102, 260–269. doi:10.1016/j.conbuildmat.2015.10.172

Keulen, A., Yu, Q. L., Zhang, S., and Grünewald, S. (2018). Effect of admixture on the pore structure refinement and enhanced performance of alkali-activated fly ash-slag concrete. *Constr. Build. Mater.* 162, 27–36. doi:10.1016/j.conbuildmat.2017.11.136

Kong, C. Y., Zhou, B., Gou, R. X., Yan, F., Wang, R., and Tang, C. X. (2023). Preparation and micromechanics of red sandstone-phosphogypsum-cement composite cementitious materials. *Materials*, 16. doi:10.3390/ma16134549

Lan, X., Gao, J. T., Qu, X. T., and Guo, Z. C. (2022). An environmental-friendly method for recovery of soluble sodium and harmless utilization of red mud: solidification, separation, and mechanism. *Resour. Conserv. Recycl.* 186, 106543. doi:10.1016/j.resconrec.2022.106543

Li, Z. F., Zhang, J., Li, S. C., Gao, Y. Y., Liu, C., and Qi, Y. H. (2020). Effect of different gypsums on the workability and mechanical properties of red mud-slag based grouting materials. *J. Clean. Prod.* 245, 118759. doi:10.1016/j.jclepro.2019.118759

Lin, R. S., Han, Y., and Wang, X. Y. (2021a). Macro–meso–micro experimental studies of calcined clay limestone cement (LC3) paste subjected to elevated temperature. *Cem. Concr. Compos.* 116, 103871. doi:10.1016/j.cemconcomp.2020.103871

Lin, R. S., Park, K. B., Wang, X. Y., and Zhang, G. Y. (2020). Increasing the early strength of high-volume Hwangtoh–cement systems using bassanite. *J. Build. Eng.* 30, 101317. doi:10.1016/j.jobe.2020.101317

Lin, R. S., Wang, X. Y., and Yi, H. (2021b). Effects of cement types and addition of quartz and limestone on the normal and carbonation curing of cement paste. *Constr. Build. Mater.* 305, 124799. doi:10.1016/j.conbuildmat.2021.124799

Liu, S. H., and Wang, L. (2018). Investigation on strength and pore structure of supersulfated cement paste. *Mater. Sci.* 24, 319–326. doi:10.5755/j01.ms.24.3.18300

Liu, S. H., Wang, L., and Yu, B. Y. (2019). Effect of modified phosphogypsum on the hydration properties of the phosphogypsum-based supersulfated cement. *Constr. Build. Mater.* 214, 9–16. doi:10.1016/j.conbuildmat.2019.04.052

Liu, Y. T., Zhang, D. R., You, L. G., Luo, H., and Xu, W. (2022). Recycling phosphogypsum in subbase of pavement: treatment, testing, and application. *Constr. Build. Mater.* 342, 127948. doi:10.1016/j.conbuildmat.2022.127948

Ma, F. Y., Chen, L. L., Lin, Z. W., Liu, Z., Zhang, W. C., and Guo, R. X. (2022). Microstructure and key properties of phosphogypsum-red mud-slag composite cementitious materials. *Materials.* 15, 6096. doi:10.3390/ma15176096

Ma, L. L., Zhang, X., Liu, F., Liu, Z. F., and Li, F. (2023). Strength characteristics and mechanism of red mud–fly ash stabilized coal gangue base. *J. Build. Mater.* 26 (07), 1–15. doi:10.3969/j.issn.1007-9629.2023.07.009

Ma, X. L., Tan, H. B., Hou, X., Su, X. M., Xian, Y. S., Dong, F. Q., et al. (2021). Research status and development trend of sulphuric acd co-production cement from phosphogypsum. *New. Build. Mater.* 48 (03), 71–76.

Ma, Y., Hu, J., and Ye, G. (2013). The pore structure and permeability of alkali activated fly ash. *Fuel.*104, 771–780. doi:10.1016/j.fuel.2012.05.034

Meskini, S., Samdi, A., Ejjaouani, H., and Remmal, T. (2021). Valorization of phosphogypsum as a road material: stabilizing effect of fly ash and lime additives on strength and durability. *J. Clean. Prod.* 323, 129161. doi:10.1016/j.jclepro.2021.129161

Mi, T. M., Mao, J. H., Cai, Y. H., Luo, S. Q., Wang, X. F., Xiao, M. L., et al. (2023). Application of Raman spectroscopy for detecting the repairing behaviour of microcapsules in self-healing cementitious system. *Constr. Build. Mater.* 387, 131637. doi:10.1016/j.conbuildmat.2023.131637

Pang, S. Y. (2021). Research on performance and application of alkali activated steel slag/slag cementitious material. *Shenyang Univ. Technol.* doi:10.27322/d.cnki.gsgyu.2021.000943

Peng, J. Z. (2013). A review on pore structure and properties of autoclaved aerated concrete. *Mater. Rev.* 27, 103–107+118.

Ren, J., Zhou, Q. Z., Yang, C. H., and Bai, Y. (2023). Performance and interaction of sodium silicate activated slag with lignosulfonate superplasticiser added at different mixing stages. *Cem. Concr. Compos.* 136, 104900. doi:10.1016/j.cemconcomp.2022.104900

Shu, K. Q., and Sasaki, K. (2022). Occurrence of steel converter slag and its high value-added conversion for environmental restoration in China: a review. *J. Clean. Prod.* 373, 133876. doi:10.1016/j.jclepro.2022.133876

Song, S. J., and Jennings, H. M. (1999). Pore solution chemistry of alkali-activated ground granulated blast-furnace slag11This paper was originally submitted to Advanced Cement Based Materials. The paper was received at the Editorial Office of Cement and Concrete Research on 12 November 1998 and accepted in final form on 16 November 1998. *Cem. Concr. Res.* 29, 159–170. doi:10.1016/s0008-8846(98)00212-9

Song, W. L., Zhu, Z. D., Pu, S. Y., Wan, Y., Huo, W. G., Song, S. G., et al. (2020). Efficient use of steel slag in alkali-activated fly ash-steel slag-ground granulated blast furnace slag ternary blends. *Constr. Build. Mater.* 259, 119814. doi:10.1016/j.conbuildmat.2020.119814

Vinai, R., and Soutsos, M. (2019). Production of sodium silicate powder from waste glass cullet for alkali activation of alternative binders. *Cem. Concr. Res.* 116, 45–56. doi:10.1016/j.cemconres.2018.11.008

Wan, Z. H., Zhang, W. Q., Liu, Z. C., and Wang, F. Z. (2022). Properties of carbide slag–slag composite cementitious material. *Bull. Chin. Ceram. Soc.* 41, 1704–1714. doi:10.16552/j.cnki.issn1001-1625.2022.05.015

Wang, C. Q., Chen, S., Huang, D. M., Huang, Q. C., Li, X. Q., and Shui, Z. H. (2023a). Safe environmentally friendly reuse of red mud modified phosphogypsum composite cementitious material. *Constr. Build. Mater.* 368, 130348. doi:10.1016/j.conbuildmat.2023.130348

Wang, J. Y. (2021). Study on the effect and mechanism of acetylene sludge on the properties of phosphogypsum. *Univ. Jinan*. doi:10.27166/d.cnki.gsdcc.2020.000198

Wang, L. L., Si, C. Y., Li, C., Sun, X. W., Zhou, H. H., and Guo, S. M. (2022e). Effect of potassium hydroxide-sodium water glass activator on properties of alkali-activated slag cementitious materials. *Bull. Chin. Ceram. Soc.* 41, 2654–2662+95. doi:10.16552/j.cnki.issn1001-1625.2022.08.004

Wang, X. J., Zhang, Z. L., Li, J. W., Wang, W. L., Mao, Y. P., and Song, Z. L. (2022c). Quantification of CO2 emission from the preparation and utilization of solid waste-based sulphoaluminate cementitious materials. *J. Clean. Prod.* 376, 134054. doi:10.1016/j.jclepro.2022.134054

Wang, X. Y., Qiao, J. S., Zhao, J. Y., Cai, T. M., and Liang, C. D. (2022d). Solidification of muddy soil with steel slag and ground granulated blast-furnace slag activated by calcium carbide slag. *Bull. Chin. Ceram. Soc.* 41, 733–739. doi:10.16552/j.cnki.issn1001-1625.2022.02.009

Wang, Y. B., Xu, L., He, X. Y., Su, Y., Miao, W. J., Strnadel, B., et al. (2022a). Hydration and rheology of activated ultra-fine ground granulated blast furnace slag with carbide slag and anhydrous phosphogypsum. *Cem. Concr. Compos.* 133, 104727. doi:10.1016/j.cemconcomp.2022.104727

Wang, Z. Y., Shui, Z. H., Sun, T., Lan, X. Y., Chi, H. H., and Li, Y. (2023b). Steel slag high iron phase activates excess-sulphate slag cement: effect on the coagulation and strength development. *Mater. Rep.* 37, 277–283.

Wang, Z. Y., Shui, Z. H., Sun, T., Li, X. S., and Zhang, M. Z. (2022b). Recycling utilization of phosphogypsum in eco excess-sulphate cement: synergistic effects of metakaolin and slag additives on hydration, strength and microstructure. *J. Clean. Prod.* 358, 131901. doi:10.1016/j.jclepro.2022.131901

Wu, B., Zhang, B., Guo, Y. F., and Peng, T. (2018). Correlation analysis of compressive strength and flexural strength of cement mortar. *J. North China Univ. Sci. Technol. Nat. Sci. Ed.* 40, 59–63.

Xu, C. W., Ni, W., Li, K. Q., Zhang, S. Q., and Xu, D. (2021). Activation mechanisms of three types of industrial by-product gypsums on steel slag–granulated blast furnace slag-based binders. *Constr. Build. Mater.* 288, 123111. doi:10.1016/j.conbuildmat.2021.123111

Yang, J., Zeng, J. Y., He, X. Y., Zhang, Y. N., Su, Y., and Tan, H. B. (2022). Sustainable clinker-free solid waste binder produced from wet-ground granulated blast-furnace slag, phosphogypsum and carbide slag. *Constr. Build. Mater.* 330, 127218. doi:10.1016/j.conbuildmat.2022.127218

Ylmén, R., Jäglid, U., Steenari, B. M., and Panas, I. (2009). Early hydration and setting of Portland cement monitored by IR, SEM and Vicat techniques. *Cem. Concr. Res.* 39, 433–439. doi:10.1016/j.cemconres.2009.01.017

You, N. Q., Li, B. L., Cao, R. L., Shi, J. J., Chen, C., and Zhang, Y. M. (2019). The influence of steel slag and ferronickel slag on the properties of alkali-activated slag mortar. *Constr. Build. Mater.* 227, 116614. doi:10.1016/j.conbuildmat.2019.07.340

Zhang, J. G., Huang, Z. W., Su, X. D., Chen, Y., Li, H. J., and Li, W. (2023). Effect of phosphogypsum addition on properties of red mud–phosphogypsum composites. *China Nonferrous Metall.* 52, 121–130. doi:10.19612/j.cnki.cn11-5066/tf.2023.01.016

Zhang, N., Liu, X. M., Sun, H. H., and Li, L. T. (2010). Pozzolanic behaviour of compound-activated red mud-coal gangue mixture. *Cem. Concr. Res.* 41, 270–278. doi:10.1016/j.cemconres.2010.11.013

Zhang, S. Y., and Wang, Q. (2021). Inhibition mechanisms of steel slag on the early-age hydration of cement. *Cem. Concr. Res.* 140, 106283. doi:10.1016/j.cemconres.2020.106283

Zhang, W., Hao, X. S., Wei, C., Liu, X. M., and Zhang, Z. Q. (2022). Activation of low-activity calcium silicate in converter steelmaking slag based on synergy of multiple solid wastes in cementitious material. *Constr. Build. Mater.* 351, 128925. doi:10.1016/j.conbuildmat.2022.128925

Zhang, Y. L., Liu, X. M., Xu, Y. T., Tang, B. W., Wang, Y. G., and Mukiza, E. (2019). Synergic effects of electrolytic manganese residue-red mud-carbide slag on the road base strength and durability properties. *Constr. Build. Mater.* 220, 364–374. doi:10.1016/j.conbuildmat.2019.06.009

Zhao, D. Q., Zhang, B. L., Shen, W. G., Wu, M. M., Guan, Y. C., Wu, J. L., et al. (2021). High industrial solid waste road base course binder: performance regulation, hydration characteristics and practical application.*J. Clean. Prod.* 313, 127879. doi:10.1016/j.jclepro.2021.127879

Zhao, J. H., Li, Z. H., Wang, D. M., Yan, P. Y., Luo, L., Zhang, H. W., et al. (2023). Hydration superposition effect and mechanism of steel slag powder and granulated blast furnace slag powder. *Constr. Build. Mater.* 366, 130101. doi:10.1016/j.conbuildmat.2022.130101

Zhou, L. B., Chen, P., Hu, C., Rong, B. G., Zhang, J., Liang, X., et al. (2023). Hydration hardening characteristics of steel slag–red mud–cement based composite mortar. *Bull. Chin. Ceram. Soc.* 42, 2837–2845. doi:10.16552/j.cnki.issn1001-1625.20230614.002

Zhu, C. F., Tan, H. B., Du, C., Wang, J., Deng, X. F., Zheng, Z. Q., et al. (2023). Enhancement of ultra-fine slag on compressive strength of solid waste-based cementitious materials: towards low carbon emissions. *J. Build. Eng.* 63, 105475. doi:10.1016/j.jobe.2022.105475